Journal of the European Ceramic Society 7 (1991) 109–116

Cathodoluminescence Measurement of Strained Alumina Single Crystals

Claudia P. Ostertag, Lawrence H. Robins & Lawrence P. Cook

National Institute of Standards and Technology, Ceramics Division, Gaithersburg, MD 20899, USA

(Received 6 August 1990; accepted 24 October 1990)

Abstract

Alumina single crystals indented with a Vickers hardness indenter were investigated by cathodoluminescence (CL) imaging and spectroscopy in a scanning electron microscope. The spatial resolution of the CL images was approximately 0·4 μm. CL spectra were measured with wavelength resolution of 1·0 nm in the wavelength range of 200 to 900 nm; in the immediate region of the ruby lines (693 nm), spectra were measured with a resolution of 0·15 nm. Stress-induced frequency shifts of the ruby lines were utilized to measure the residual stresses in the region surrounding the indentation. Both hydrostatic and non-hydrostatic stresses were measured. The magnitude of the stresses was observed to vary with distance from the center of the indent and also with crystallographic orientation. After the samples were annealed at 1600°C for 10 h, no measurable stresses remained either in the center of the indent or in the surrounding area.

Al_2O_3-Einkristalle wurden mit einem Vickers Härteeindruck versehen und mit einem Kathodenlumineszensverfahren (KL) in einem Rasterelektronenmikroskop untersucht. Die laterale Auflösung des KL-Signals betrug ca. *0·4 μm. Die KL-Spektren wurden im Wellenlängenbereich von 200 nm bis 900 nm mit einer Auflösung von 1·0 nm aufgenommen. Im Bereich der Rubinlinie (693 nm) wurde das Spektrum mit einer Auflösung von 0·15 nm gemessen. Die Restspannungen im Bereich der Härteeindrücke wurden durch spannungsabhängige Frequenzverschiebungen der Rubinlinie gemessen. Es wurden sowohl hydrostatische wie auch nicht-hydrostatische Spannungen gemessen. Die beobachteten Spannungswerte variierten sowohl mit der Entfernung vom Zentrum des Härteeindrucks als auch mit der kristallographischen Richtung. Nach einer zehnstündigen Wärmebehandlung bei 1600°C waren in den Proben weder im Zentrum des Härteeindrucks noch in dessen Umgebung Spannungen meßbar.*

On a étudié à l'aide de l'imagerie par cathodoluminescence (CL) et par spectroscopie dans un microscope à balayage des monocristaux d'alumine indentés par méthode de dureté Vickers. La résolution spatiale des images CL était approximativement de 0·4 μm. Les spectres CL étaient mesurés avec une résolution de longueur d'onde de 1·0 nm dans un domaine de longueur d'onde allant de 200 à 900 nm; à proximité des raies du rubis (693 nm) les spectres étaient mesurés avec une résolution de 0·15 nm. Les déplacements de fréquence des raies du rubis induits par les contraintes ont été utilisés pour évaluer les contraintes résiduelles dans la région environnant l'indentation. On a mesuré les contraintes hydrostatiques et non-hydrostatiques. On a constaté que l'intensité des contraintes variait en fonction de la distance au centre de l'indent ainsi qu'avec l'orientation cristallographique. Après un recuit de 10 heures à 1600°C il ne subsiste plus de contraintes mesurables, aussi bien au centre de l'indent que dans la région périphérique.

1 Introduction

Residual stresses are present in both monolithic and composite materials and have a strong influence on their mechanical properties. For example, the increasing resistance to crack propagation with crack length (*R*-curve behavior) in alumina is attributed to the interlocking grains which are clamped into the matrix on either side of the crack interface by internal thermal expansion mismatch

Journal of the European Ceramic Society 0955-2219/91/$3.50

stresses.[1] In composite materials the toughness depends strongly on the residual stresses (clamping stress) between reinforcement and matrix, and hence recent discussions yield the need to assess the effects of the residual stress field on the fiber debonding.[2,3] Knowledge of these stresses, specifically their magnitude, is of importance. Unfortunately, there are few non-destructive techniques that measure residual stresses in bulk ceramic materials with high spatial resolution.

The feasibility of using cathodoluminescence as a non-destructive technique to measure residual stresses with high spatial resolution was investigated. Cathodoluminescence (CL) is the phenomenon of light emission from specimens as a result of interaction with an electron beam. In insulating crystals, the origin of the luminescence arises from impurity atoms (e.g. transition metals or rare earths) in the crystal lattice. Using an electron microscope to produce the electron beam, the spatial distribution of luminescent sites can be observed with submicron spatial resolution, and correlated with features of the specimen morphology or microstructure. To illustrate the technique single crystal sapphire disks were indented by a Vickers hardness indenter and the residual stresses around the indentation measured through the stress-induced frequency shifts of the ruby lines. Furthermore, changes in the CL of the single-crystal sapphire disk caused by deformation of the crystal were investigated.

2 Physical Processes that Lead to Cathodoluminescence

The mechanisms for CL are similar to those for photoluminescence, but the energy input or excitation source is that of an electron beam rather than a visible or ultraviolet light beam. When an energetic (keV range) electron beam propagates within a semiconductor or insulator, the primary electrons lose energy by the creation of electron–hole pairs. These electron–hole pairs then recombine via radiative and non-radiative processes. Only the radiative recombination process which leads to the creation of a photon is viewed with CL. Radiative recombination may be intrinsic (arising from electronic states of the perfect crystal) or extrinsic (arising from electronic states that are localized at defects or impurities in the crystal). Extrinsic luminescence thus provides information about defects and impurities in the crystal lattice. For conciseness, the defects and impurities that give rise to extrinsic luminescence are often denoted the luminescence centers. Each type of luminescence center in a particular crystal has a characteristic emission spectrum. The spectrum may contain both narrow lines and broad bands, depending on the energy level structure of the luminescence center and the coupling of the center to the host lattice.

3 Piezospectroscopic Effects in $Al_2O_3:Cr^{3+}$

In oxide insulators, a number of transition metal and rare earth impurities act as luminescence centers. The trivalent chromium ion (Cr^{3+}), with electronic configuration $3d^3$, is an efficient luminescence center in many light-metal oxides, including Al_2O_3 and MgO. The trivalent chromium ion enters substitutionally and is surrounded by an octahedron of oxygen ions. A chromium ion in a cubic crystal such as MgO has a single resonance line corresponding to the ^2E–$^4A_2$ transition. This is called the ruby (R) line as it appears in the red region near 7000 Å. In aluminum oxide, the surroundings of the chromium ion are not quite cubic, as the oxygen octahedron is stretched along its trigonal symmetry axis C_3. The trigonal symmetry of the Cr^{3+} ion induces a splitting of the upper ^2E level by 29 cm^{-1}, giving rise to two distinct transition R lines, R_1 and R_2 at 14 402·5 cm^{-1} and 14 432·1 cm^{-1}, respectively. The lower $4A_2$ level is also split by the trigonal field, but the splitting of 0·38 cm^{-1} is too small to be resolved under most conditions.

An applied or residual stress distorts the positions of the atoms surrounding the Cr^{3+} impurity ion. For example, a hydrostatic compressive (tensile) stress will change the crystal field seen by the chromium ion by reducing (increasing) the bond lengths between the oxygen and the chromium ions and hence changing the energies of the radiative transitions. This change in energies is detected as a frequency shift of the ruby lines. A hydrostatic stress causes the R_1 and R_2 lines to shift to lower energies by virtually equal amounts.[4] Non-hydrostatic stresses cause the R_1 and R_2 lines to shift by unequal amounts.[5,6] For example, a compressive uniaxial stress along the trigonal axis (C_3) makes the environment closer to cubic, and thus reduces the splitting of the ^2E level and of the R_1 and R_2 lines. A compressive uniaxial stress perpendicular to the C_3 axis makes the environment farther from cubic and increases the ^2E splitting (but by approximately half as much as compression parallel to C_3 reduces the splitting).[5]

The use of the ruby line shifts to determine

residual stresses in alumina ceramics was first demonstrated by Grabner.[7] The stress state of a crystal subjected to a uniform deformation can be described with the help of six components of the stress tensor, the normal stresses ($\sigma_{11}, \sigma_{22}, \sigma_{33}$) and the shear stresses ($\sigma_{12}, \sigma_{13}, \sigma_{23}$). For relatively small stresses, only linear terms need to be included in the expression for displacement of the energy levels as a function of stress. The approximate condition for the linear approximation to be valid is that the changes in the atomic positions are small compared to the equilibrium (unstressed) interatomic distances. In practice, this condition always holds, because the crystal will fracture before the changes in atomic positions can become large. Hence, if it is assumed that the displacements (shifts) of the energy levels of the impurity centers (chromium ions) are linear functions of the stress components in a uniformly deformed lattice, one can write:

$$\Delta\nu = \pi_{11}\sigma_{11} + \pi_{22}\sigma_{22} + \pi_{33}\sigma_{33} + \pi_{12}\sigma_{12} + \pi_{13}\sigma_{13} + \pi_{23}\sigma_{23} \quad (1)$$

or in contraction notation:

$$\Delta\nu = \pi_{ij}\sigma_{ij}$$

where $\Delta\nu = \nu - \nu_0$ is the frequency shift of the ruby lines (ruby line position for stressed material (ν), ruby line position when unstressed (ν_0)). (π_{ij}) are the piezospectroscopic coefficients relating the change in frequency to the stress state.

Let the stress tensor (σ_{ij}) be expressed in the system of coordinates associated with the high symmetry directions of the lattice surrounding the impurity ion. Group theory considerations show that for an ion in a high symmetry environment, some coefficients are zero and other coefficients are equal to each other. In a cubic environment, there is only one coefficient, $\pi_{11} = \pi_{22} = \pi_{33}$. For an ion in an environment of trigonal symmetry, there are two independent coefficients, $\pi_{11} = \pi_{22}$ and π_{33}; all other coefficients are zero. Thus eqn (1) can be written:

$$\Delta\nu = \pi_{11}(\sigma_{11} + \sigma_{22}) + \pi_{33}\sigma_{33} \quad (2)$$

The frequency shift induced by hydrostatic stress (pressure P) is given by the sum $(2\pi_{11} + \pi_{33})$. This sum of coefficients has been measured to high accuracy by Munro *et al.*[4] and the values for the R_1 and R_2 lines are $7{\cdot}59\,\mathrm{cm}^{-1}\,\mathrm{GPa}^{-1}$ and $7{\cdot}615\,\mathrm{cm}^{-1}\,\mathrm{GPa}^{-1}$ respectively.

It is often more convenient to divide the stress into hydrostatic and non-hydrostatic components and write eqn (1) as follows:

$$\Delta\nu = (2\pi_{11} + \pi_{33})P + (\pi_{33} - \pi_{11})S \quad (3)$$

where P is the hydrostatic component $(\sigma_{11} + \sigma_{22} + \sigma_{33})/3$ and S is the non-hydrostatic component $(2\sigma_{33} - \sigma_{11} - \sigma_{22})/3$.

The individual coefficients π_{11} and π_{33} have been measured to lower than $(2\pi_{11} + \pi_{33})$ accuracy by uniaxial stress experiments with single crystals by Schawlaw[5] and Kaplianskii.[6]

The line shift can also be expressed in the stress coordinate frame, in cases where the stresses are referred to their principal axis (eqn (4)) or Love frame (eqn (5)), by transforming the piezospectroscopic tensor into the stress frame:

$$\Delta\nu = 3\pi_{11}P + (\pi_{33} - \pi_{11}) \times [p_{13}^2\sigma_{11} + p_{23}^2\sigma_{22} + p_{33}^2\sigma_{33}] \quad (4)$$

or:

$$\Delta\nu = (2\pi_{11} + \pi_{33})P + (\pi_{33} - \pi_{11}) \times [p_{13}^2(\sigma_{11} - P) + p_{23}^2(\sigma_{22} - P) + p_{33}^2(\sigma_{33} - P)] \quad (4a)$$

$$\Delta\nu = 3\pi_{11}P + (\pi_{33} - \pi_{11})P \times [l_{13}^2 + l_{23}^2 + l_{33}^2] + 2(\pi_{33} - \pi_{11}) \times [l_{13}l_{23}\sigma_{12} + l_{13}l_{33}\sigma_{13} + l_{23}l_{33}\sigma_{23}] \quad (5)$$

or:

$$\Delta\nu = (2\pi_{11} + \pi_{33})P + 2(\pi_{33} - \pi_{11}) \times [l_{13}l_{23}\sigma_{12} + l_{13}l_{33}\sigma_{13} + l_{23}l_{33}\sigma_{23}] \quad (5a)$$

where the matrices p_{ij} and l_{ij} refer to the orthogonal transformation between the crystal structure coordinates and the stress tensor coordinates σ_{ij}. Equations (4a) and (5a) are preferable because they express the peak shift in terms of the quantities measured with high accuracy, namely $(2\pi_{11} + \pi_{33})$.

When the stress tensor is given in an arbitrary coordinate frame relative to the crystal frame, the line shift is given by the relation:

$$\Delta\sigma = (2\pi_{11} + \pi_{33})P + (\pi_{33} - \pi_{11}) \times [a_{13}^2(\sigma_{11} - P) + a_{23}^2(\sigma_{22} - P) + a_{33}^2(\sigma_{33} - P)] + 2(\pi_{33} - \pi_{11}) \times [a_{23}a_{33}\sigma_{32} + a_{13}a_{23}\sigma_{21} + a_{13}a_{33}\sigma_{31}] \quad (6)$$

The R_1 and R_2 lines form a pair of overlapping bell-shaped curves. The peak positions of the R_1 and R_2 lines can best be obtained from the numerical data by fitting analytical functions to the two bell-shaped curves. The most widely known bell-shaped functions, Gaussian and Lorentzian, do not accurately fit the observed lineshapes of the R lines. Therefore, the R lines are represented by a more general bell-shaped function equation:

$$I(\nu - \nu_0) = G(\nu - \nu_0; w_1) \cdot [L(\nu - \nu_0; w_2)]^{\beta} \quad (7)$$

where G is a Gaussian of width w_1, L is a Lorentzian of width w_2, and β is an exponent greater than zero.

4 Experimental Procedure

Single crystal sapphire disks with off-a-axis $(11\bar{2}0)$ orientations (orientation was determined by Laue back reflection) were indented by a diamond Vickers hardness indenter under a load of 2N. The quadrants of the indent were oriented approximately parallel to the [0001] (three-fold symmetry direction) and $[\bar{1}010]$ directions of the crystal. Both radial and lateral cracks were observed in the optical microscope. CL was excited by a scanning electron microscope (SEM). Broadband CL images, spectrally resolved CL images and secondary-electron images of the indent and the surrounding region were obtained. High-wavelength-resolution CL spectra of the R lines were measured for a number of different areas ($5\,\mu m^2$) within the indent and surrounding region. Low-wavelength-resolution CL spectra (wavelength range 200 to 900 nm) were taken in the center of the indent, next to the indent, and in an undamaged region far from the indent. For spectroscopic measurements, the electron beam voltage was 20 keV and the beam current was approximately 10^{-9} A. After the initial CL measurements were completed, the sapphire discs were annealed at 1600°C for 10 h and the CL measurements were repeated.

To avoid distortion of the spectra caused by chromatic aberration, only reflecting optics were used in the CL collection system. The CL from the specimen was initially collimated by a concentric pair of spherical concave and convex mirrors and transmitted through a fused silica window. For CL imaging the luminescence was detected by a photomultiplier tube (PMT) placed close to the window and the detector signal was then sent to the image-production system of the SEM. Spectrally resolved CL imaging was accomplished by placing an optical interference filter in front of the PMT, which had an S20 spectral response. The interference filters had center wavelengths from 400 to 850 nm and bandwidths of 40 nm. For CL spectroscopy the luminescence was focused onto the entrance slit of a 0·34 m monochromator by a second pair of mirrors (one flat, the second concave). The spectrally dispersed light in the exit plane of the monochromator was detected by an optical multichannel analyzer (OMA), which consists of a microchannel plate intensifier and 700-element silicon photodiode array. The OMA has a spectral response similar to a red-enhanced S20 PMT. Spectral data from the multichannel analyzer were transferred to a computer for storage, display and further analysis. CL spectra could be measured with the monochromator and OMA in a spectral range from 1·4 to 6·0 eV. Two sets of gratings were used; for low-resolution, wide-range spectra, 300 line/mm gratings blazed at 300 nm and 500 nm were used. Spectral resolution with these gratings was 1 nm. For high-resolution, narrow-range spectra, 1800 line/mm holographic gratings provided a spectral resolution of 0·15 nm. Wavelength calibrations were carried out with a set of atomic-vapor lamps. A Krypton lamp was used to calibrate the spectra in the region of the R lines (693 nm). By recording wavelength-calibration spectra just before and just after the experimental spectra, to compensate for the slight wavelength drift of the multichannel detector, wavelengths were measured with an accuracy and precision of at least 0·01 nm (which corresponds to $0{\cdot}2\,cm^{-1}$ at 693 nm).

It should be noted that in this system, separate ports are used for CL and for secondary-electron (SE) collection. Thus, the secondary-electron image can be obtained at the same time as the CL image and spectrum, without moving the specimen, allowing the SE and CL images of the same sample region to be readily obtained.

5 Results

5.1 CL imaging and CL spectra of indented region

The secondary electron micrograph of the indent is shown in Fig. 1(a) and the corresponding CL image is shown in Fig. 1(b). The secondary electron micrograph shows the microstructural features such as the radial cracks which radiate from the corners of the indent and the lateral crack to the right of the indent. Bright haloes around the indentation quadrants are observed in the CL image. It should be noted that in Fig. 1(b) the center of the indent is completely non-luminescent. After prolonged excitation of the sample by the electron beam, however, the center of the indent became partly luminescent and, furthermore, the CL image contrast in the haloes around the indent was enhanced. After annealing the sample at 1600°C for 10 h, the CL image contrast, both in the center of the indent and in the surrounding region, was greatly reduced. Similar features were observed by other researchers around indentations in magnesia.[8-11] Although deformation zones in MgO produce striking image contrast when observed by CL in the electron microscope, the origin of the image contrast is not

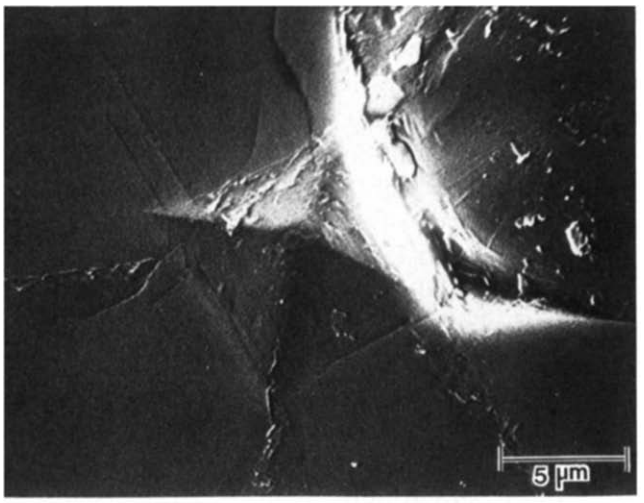

(a)

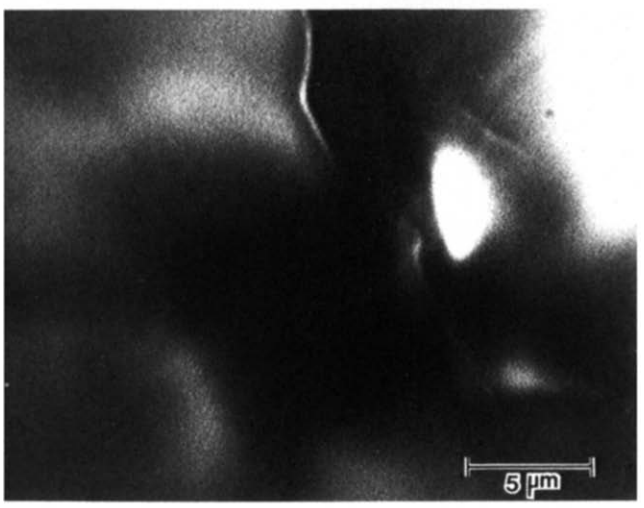

(b)

Fig. 1. Secondary electron micrograph (a) and corresponding CL image (b) of a 200 g Vickers hardness indentation in (11$\bar{2}$0) surface of sapphire. Note that the center of the indent is non-luminescent.

well understood and has been a subject of controversy. The image contrast will be discussed in more detail in Section 6.

To investigate the origin of the observed CL, low-resolution CL spectra of 5 μm^2 regions far from the indent (undeformed region), in the center of the indent and close to the indent (inside the lateral crack, where a bright halo was observed) were obtained. The CL spectra are shown in Fig. 2, where CL intensity is plotted as a function of photon energy. The 3·8 eV CL band was the most intense band for each of the three regions. This 3·8 eV band is attributed to F^+-centers (oxygen-ion vacancies occupied by one electron).[12] A broad 1·6 eV band and the narrow R lines of the chromium impurity atoms at 1·79 eV (which appear to be a single narrow line at this low resolution) are seen in two of the regions, but are completely quenched in the center of

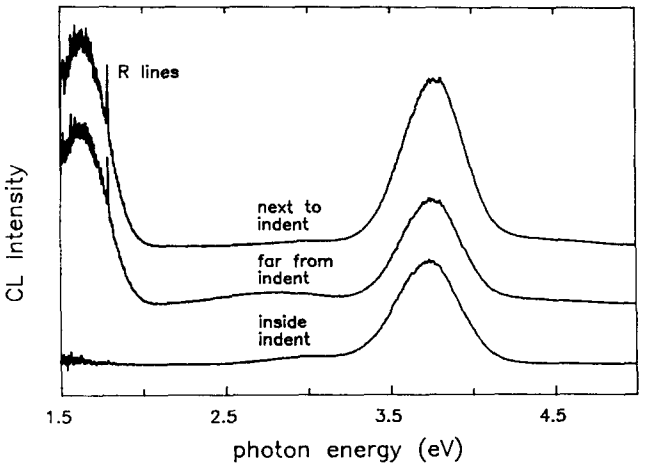

Fig. 2. Low-resolution cathodoluminescence spectra from different regions of the sapphire disk; (a) in center of the indent, (b) far from indent and (c) in highly luminescent region next to indent.

the indent. This correlation suggests that the 1·6 eV band may also arise from chromium ions, possibly in association with an unidentified lattice defect. Chromium ions give rise to a broad 1·5–1·6 eV band when they exist at low-crystal-field sites, as in most glasses. The same features are seen in the CL spectra of the deformed and undeformed regions; it thus appears that the indentation created no new CL centers. However, an increase in the CL intensity was observed for the F^+-band (3·8 eV), the 1·6 eV band and the R lines when the CL spectrum was taken inside the ring crack next to the indent. This increase in intensity suggests an increase in the number of CL centers, or an increase in the efficiency of excitation of previously existing centers (e.g. by energy transfer from another type of defect created by the deformation). An increase in the number of CL centers is possible, but this is unlikely to occur for an isolated impurity center.

5.2 CL residual stress measurements

For the residual stress measurements the shift in the peak positions of the R_1 and R_2 lines was investigated. The ruby line positions R_1 and R_2 are a function of the Cr^{3+}-ion displacements in the lattice. Changes in the linewidths of R_1 and R_2 can in principle provide information about the stress distribution within the probed region, but to study stress-induced line broadening, it is necessary to cool the sample to eliminate the large thermal phonon broadening present at room temperature. Figure 3 shows high-resolution CL spectra in the R line region taken in the center of the indent, near the indent and far from the indent. Far from the indent the material is undeformed; hence the peak values of the R_1 and R_2 lines far from the indent are taken to

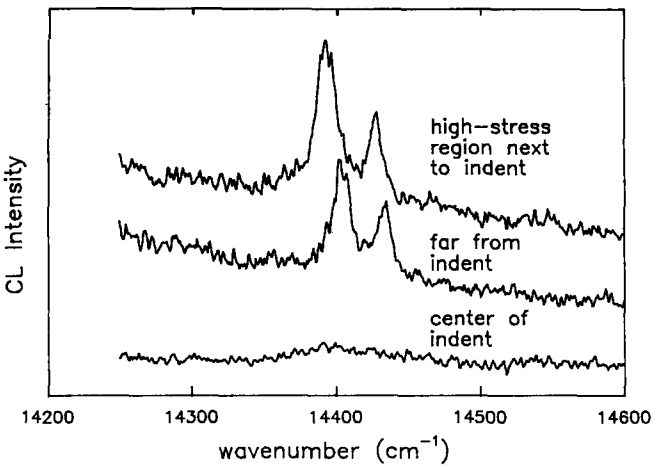

Fig. 3. High-resolution cathodoluminescence spectra of ruby (Cr^{3+} impurity) lines taken (a) in center of the indent, (b) far from indent and (c) in the high stress region next to the indent.

be the reference values for unstressed material. The necessity of making a further correction for the temperature dependence of the peak positions is thereby avoided, because the sample temperature can be assumed to be the same for nearly simultaneous measurements near and far from the indent. As mentioned before, the R lines are quenched in the center of the indent and therefore the stresses in the center of the indent cannot be determined. The R lines next to the indent show a shift to lower wavelengths which is associated with a compressive residual stress field.

The residual stresses were determined from the measured ruby line positions along three different directions as a function of distance from the indent. Two of the measured directions parallel to the indent quadrants correspond approximately to the crystallographic directions [0001] and [$\bar{1}$010]. Figure 4 indicates the areas selected for the measurement of the residual stresses. These areas are readily detectable in a secondary-electron image obtained subsequent to the CL because of beam-induced damage to the surface or near-surface region. In the case of a pure hydrostatic stress both ruby lines R_1 and R_2 shift by approximately equal amounts, but under non-hydrostatic stress the two ruby lines may shift unequally, depending on the orientation of the stress. The hydrostatic and the non-hydrostatic stresses were determined from eqn (3) for the R lines R_1 and R_2. The results are plotted in Fig. 5(a) (hydrostatic stress) and Fig. 5(b) (non-hydrostatic stress). For convenience, eqn (3) is rewritten here using the experimentally determined coefficients $(2\pi_{11} - \pi_{33})$ from Munro *et al.*[4] and the $(\pi_{33} - \pi_{11})$ coefficients from taking the average of

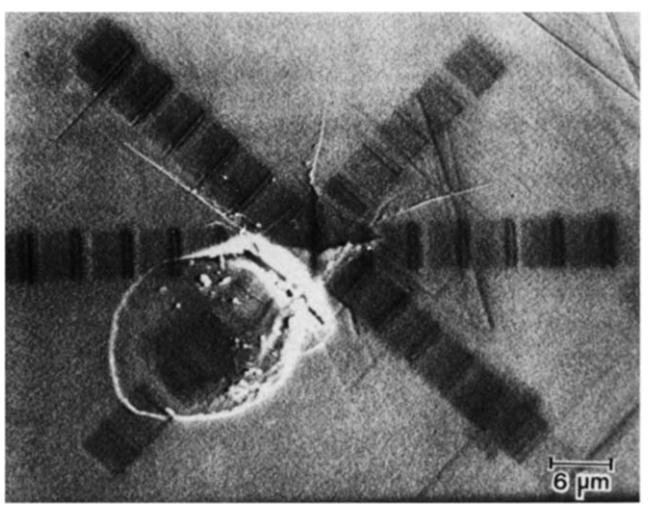

Fig. 4. Secondary-electron image of the selected areas along which the frequency shifts of the R_1 and R_2 peaks were measured as a function of distance from the center of the indent. The raster size is approximately $5 \times 5\,\mu m^2$.

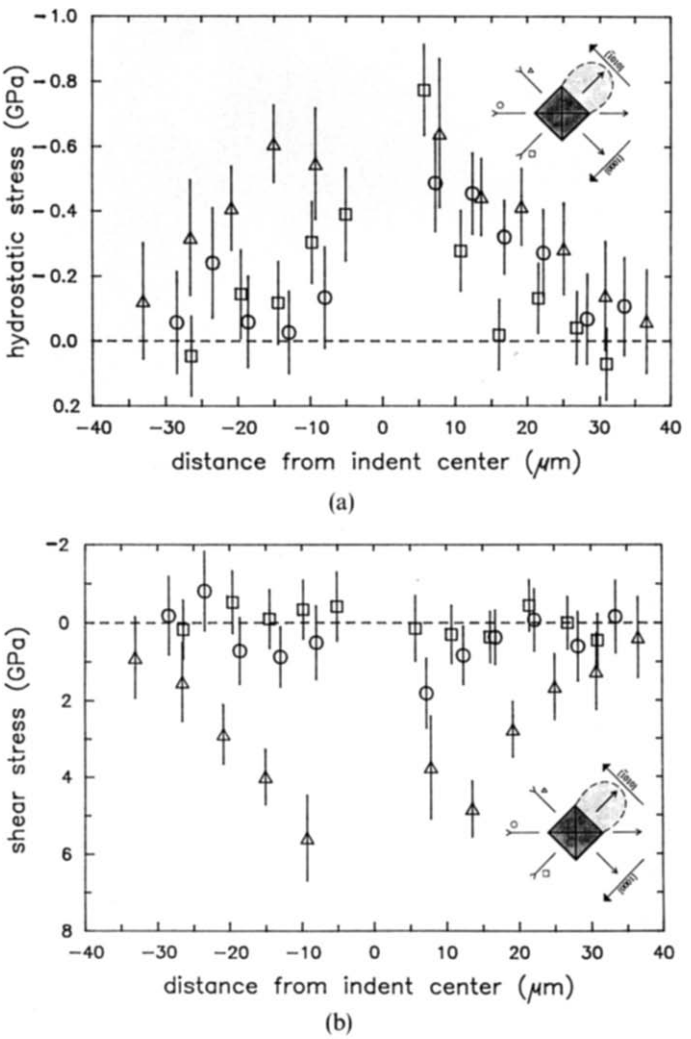

Fig. 5. Hydrostatic and shear stresses induced by the Vickers indent as a function of distance from the center of the indent and as a function of crystallographic orientation; the hydrostatic (a) and the shear stresses (b) were obtained from the frequency shifts of the ruby lines. Negative values indicate compression, positive values tension.

the measurements made by Schawlow[5] and Kaplianskii.[6]

$$\begin{aligned} &\text{Ruby line } R_1\text{: } \Delta\nu = 7{\cdot}590\,.\,P - 1{\cdot}5\,.\,S \\ &\text{Ruby line } R_2\text{: } \Delta\nu = 7{\cdot}615\,.\,P - 0{\cdot}6\,.\,S \end{aligned} \quad (8)$$

Each point in Fig. 5(a) and (b) corresponds to the measured average stress in one of the selected 5 μm^2 areas. The residual stresses, both hydrostatic and non-hydrostatic, decrease as a function of increasing distance from the center of the indent. It can be seen that the stress distributions are also highly anisotropic.

After annealing the sample at 1600°C for 10 h, no residual stresses remained either inside or next to the indentation and crack healing was observed. (The previously quenched R lines inside the central indentation area reappeared after annealing; it was thus possible to determine that there were no observable stresses in the central area after annealing).

6 Discussion

6.1 CL imaging and spectra

The action of the indenter produces non-uniform plastic deformation and hence leaves a residual stress field in the region of the indent. As seen in Fig. 2, there are a number of luminescence centers present in the undeformed sapphire used in this study: F^+-centers (3·8 eV band), Cr^{3+} ions, and other unidentified centers (e.g. the 1·6 eV band which may arise from a chromium-defect complex). Initially, the strong deformation in the center of the indent causes complete quenching of the CL. However, with prolonged electron-beam irradiation, the F^+-center (3·8 eV) CL is partially restored within the indent, but the R lines and the 1·6 eV band remain quenched. It is known that luminescence is quenched by concentrations of sensitizing and activating impurities in excess of several percent.[13] So it is not surprising that crystals which become more luminescent as a result of plastic deformation lose their luminescence when the deformation is too severe. The regions surrounding the indent show a greater intensity in all of the CL bands than the undeformed crystal. An increase in CL intensity is associated with an increase in the number of CL centers or in the efficiency of excitation or radiative recombination of these centers. It is possible that additional F^+-centers and other luminescent defects are produced during deformation. Another possibility is that new types of defects are created, which are themselves non-luminescent, which increase the excitation or radiative efficiency of recombination at the existing CL centers by an energy transfer process. This seems necessary to explain the increase in the R line luminescence, because the indentation cannot create more chromium atoms.

An indentation process produces both dislocations and point defects. Studies of Vickers indentations in single-crystal MgO attributed the CL image contrast around the indents to either point defects[8,14,15] or dislocations.[9,16] Hockey[17] provides direct evidence that high densities of dislocations are produced under hardness indentations in sapphire single crystals. It is possible that the enhancement of CL intensity around the indent is due to dislocations, since it is known from research on Te-doped GaAs that dislocations can locally enhance the CL intensity.[18] A luminescence center such as the F^+-center may have different trapping and recombination properties when it is near a dislocation core than when it is in a defect-free region, giving rise to CL image contrast. Point defects such as F^+-centers may be generated by the intersection of dislocations. Any of the above mechanisms might be responsible for the enhanced intensity of the luminescence observed near the indentations, as seen in Fig. 1(b).

6.2 Residual stress measurements

The compressive stress inside the indent were theoretically assessed using Hill's approximation of a spherical inclusion in an infinite medium,[19] where the pressure P inside the cavity is a function of the elastic modulus E, the yield stress Y and Poissons ratio ν:

$$P = 2Y/3\,.\,\{1 + \ln[E/3(1-\nu)Y]\} \quad (9)$$

where E/Y is obtained by combining the following two equations:

Marsh equation:[20]

$$H/Y = 0{\cdot}28 + \{0{\cdot}6/[1 - 1{\cdot}2(Y/E)]\} \times \ln\{(E/Y)/[2{\cdot}4 - 1{\cdot}44(Y/E)]\} \quad (10)$$

and

$$H/Y = H/E\,.\,E/Y \quad (11)$$

where H is the hardness and H/E for sapphire is 20 GPa/425 GPa. The pressure inside a spherical cavity for sapphire is calculated from eqn (9) to be 25 GPa and, according to Hill, the stress decreases as $1/r^3$ with distance r away from the center of the cavity. The hydrostatic stress field for the theoretically determined pressure of 25 GPa is compared with the experimental results in Fig. 6. Hill's equation is derived for an isotropic material, however, while alumina is highly anisotropic. The

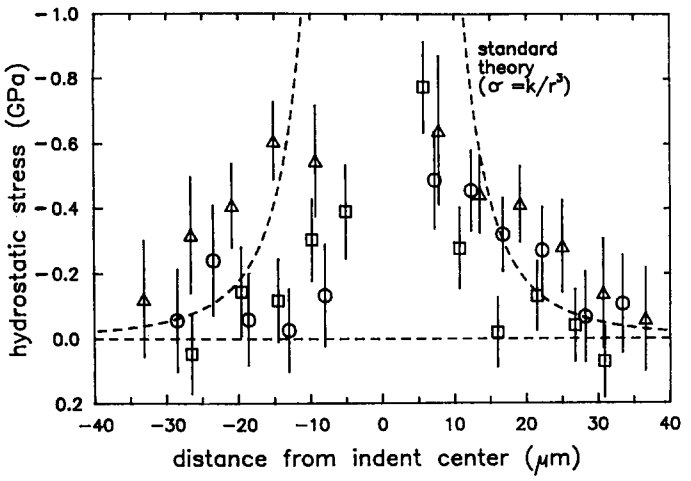

Fig. 6. Plot of the experimentally observed and theoretically determined stress decrease (for theoretically determined pressure of 25 GPa) as a function of distance from the center of the indent.

residual stresses measured in different directions reveal this anisotropy. The lowest residual stresses were observed along the [0001] direction. The largest stresses were obtained along the [$\bar{1}$010] direction. One possible explanation for the higher stresses in the latter direction is the presence of basal twins, as observed in the optical and SEM micrographs. Instead of cracks, twin planes formed in the [$\bar{1}$010] directions, as can be seen in the upper left corner and the bottom right corner of Fig. 1(a). Crack formation along {0001} planes in alumina is most unlikely due to the charge neutrality. Due to the twin planes, higher residual stresses remain, whereas in the other directions, the residual stresses are relaxed by the formation of cracks. Comparison of Fig. 5(a) with Fig. 5(b) shows that non-hydrostatic stresses are relaxed more completely than hydrostatic stresses by crack formation.

7 Concluding Remarks

Cathodoluminescence imaging and spectra were used to study strained alumina single crystals. Furthermore, the CL technique was utilized as a tool to measure residual stresses around a Vickers indentation in a sapphire crystal. The technique is capable of measuring the residual stresses with high precision and with a spatial resolution of better than 5 μm. For future studies, it should be possible to increase the precision of the stress measurements by cooling the sample to liquid nitrogen temperature, thereby increasing the sharpness of the ruby lines by reducing thermal broadening. Measurement of stresses through the frequency shifts of the R lines enables the hydrostatic stress and one component of the non-hydrostatic stress to be obtained. The hydrostatic stress was measured to a precision of $\pm$0·2 GPa and the non-hydrostatic stress to $\pm$0·1 GPa. An improvement in the precision of stress measurement is expected in more heavily chromium-doped crystals where the R-line intensity is known to be greater.

Acknowledgements

The authors gratefully acknowledge fruitful discussions with Brian R. Lawn and Edwin R. Fuller Jr.

References

1. Bennison, S. J. & Lawn, B. R., *Acta Met.*, **37** (1989) 2659.
2. Marshall, D. B. & Evans, A. G., *J. Am. Cer. Soc.*, **68**(5) (1985) 225.
3. Luh, F. Y. & Evans, A. G., *J. Am. Cer. Soc.*, **70**(7) (1987) 466.
4. Munro, R. G., Piermarini, G. J., Block, S. & Holzapfel, W. B., *J. Appl. Phys.*, **57** (1985) 165.
5. Schawlaw, A. L., In *Advances in Quantum Electronics*, ed. J. R. Singer. Columbia University Press, NY, 1961.
6. Kaplyanskii, A. A. & Przhevuskii, A. K., *Sov. Phys. Dokl.*, **7** (1962) 37.
7. Grabner, L., *J. Appl. Phys.*, **49** (1978) 580.
8. Velednitskaya, M. A., Rohzhanskij, V. N., Comolovan, L. F., Saparon, G. V., Schreiber, J. & Brummer, O., *Phys. Status Solidi (a)*, **32** (1975) 123.
9. Pennycook, S. J. & Brown, L. M., *J. Luminesc.*, **18/19** (1978) 905.
10. Chaudhri, M. M., Hagan, J. T. & Wells, J. K., *J. Mater. Sci.*, **15** (1980) 1189.
11. Brown, L. M., Younis Khan, M. & Chaudhri, M. M., *Phil. Mag. A*, **57** (1988) 187.
12. Evans, B. D. & Stapelbroek, M., *Phys. Rev. B*, **18** (1978) 7089.
13. Dexter, D. L., *J. Chem. Phys.*, **21** (1953) 836.
14. Llopis, J., Piqueras, J. & Bru, L., *J. Mater. Sci. Lett.*, **13** (1978) 1361.
15. Enomoto, Y. & Tabor, D., *Proc. Roy. Soc. London A*, **373** (1981) 405.
16. Berger, S. D. & Brown, L. M., In *Electron Microscopy and Analysis, Conf. Series #61*, ed. M. J. Goringe. The Institute of Physics, Bristol and London, 1981, p. 473.
17. Hockey, B. J., *J. Am. Cer. Soc.*, **54**, University Press, Oxford (1971) 223.
18. Wittry, D. B. & Hyser, D. F., *J. Appl. Phys.*, **35** (1964) 2439.
19. Hill, R., *The Mathematical Theory of Plasticity*. 1950, p. 104.
20. Marsh, D. M., *Proc. Roy. Soc. London A*, **279** (1974) 420.